Peer review status:

This is a non-peer-reviewed preprint submitted to EarthArXiv.

Plastic more than brittle failure may govern standard propagation saw tests

Hamed Haftbaradaran[1,2], Mahmood Heshmati[3], Nicola M. Pugno[1,4*]

[1] Mechano-X Labs, Department of Civil, Environmental, and Mechanical Engineering, University of Trento, Trento, 38123, Italy
[2] Department of Civil Engineering, University of Isfahan, Isfahan, Iran
[3] Kermanshah University of Technology, Kermanshah, Iran
[4] School of Engineering and Materials Science, Queen Mary University of London, London, E1 4NS, UK

Abstract

Understanding standard (1 m) propagation saw test (PST) as an invaluable tool for studying failure of snowpacks has remained elusive. Although fracture mechanics theories are commonly applied for interpreting PSTs, recently performed standard PSTs under controlled conditions of slope angle/loading suggest that such theories cannot adequately explain critical cut length measurements vs. slope angle even when empirical fracture criteria are utilized. Here, we demonstrate that standard PSTs performed for a wide range of slope angles with both upslope and downslope cuts can be explained by a nonlinear plastic analysis using a simple cap failure envelope for the weak layer rather than by brittle fracture. Building on the well-established concept of brittle-to-ductile transition in structural failure mechanics, our analysis suggests that plastic collapse within the weak layer may remain the dominant mechanism well into the dimensions of standard PSTs, depending on characteristic lengths influenced by a number of factors, including elastic properties of the slab/weak layer, fracture toughness and plastic strength of the weak layer as well as the slope angle. Accordingly, a plastic-to-brittle transition is expected with increasing the size scale, thus longer PSTs are suggested to investigate the fracture properties relevant to avalanches. Importantly, this framework generalizes beyond classical weak-layer assumptions and linear elasticity, extending to conditions such as wet snow, which favor ductile behavior and are becoming increasingly relevant under climate change.

[*] Corresponding author: nicola.pugno@unitn.it

1. Introduction

Understanding snow avalanches, even in the simplest configuration of a dry snow cohesive slab resting on a weak layer, remains a major challenge. This difficulty primarily arises from limited knowledge of snow's constitutive behavior, its spatial variability, and the complex geometry of natural snowpacks. Despite these uncertainties, small-scale controlled field experiments, specifically Propagation Saw Tests (PST), provide a valuable framework for investigating failure mechanisms. Although PST has been widely used for studying weak layer failure, interpretation of the results has remained challenging, partly due to the variability of the methods used in performing the test, as factors such as cutting direction (upslope vs. downslope), slab dimensions (thickness and length), and geometry (isolated blocks in slope-normal or vertical directions) could influence the results (Bergfeld et al., 2025). As a result, reports on the trend of critical cut-length vs. slope angle have remained controversial (Gaume et al., 2017; Gauthier and Jamieson, 2008a; McClung, 2009; Sigrist and Schweizer, 2007).

To clarify such controversies, (Adam et al., 2024) conducted extensive PST experiments with an innovative setup that allowed controlled slope angle and loading adjustments and identified a clear trend for variations in critical cut length with slope angle. Since gravitational loading on an inclined surface naturally produces both normal and tangential loading, mixed-mode fracture mechanics provides a potentially powerful framework for explaining PSTs. In classical linear elastic fracture mechanics, crack propagation is predicted to occur when the combined contributions of mode I and mode II energy release rates reach a critical threshold. A commonly used mixed-mode interaction criterion assumes a linear combination of these contributions (Hutchinson and Suo, 1991). As complex material-specific mechanisms could regulate interaction of the two modes, various nonlinear mixed-mode criteria have been developed in the literature (Benzeggagh and Kenane, 1996; Mantič et al., 2015; Reeder, 1992). Adam et al., (2024) evaluated various mixed-mode fracture criteria in relation to their extensive experimental data and found that a fracture criterion based on a power-law interaction of the two modes can better explain measurements of critical cut length vs. slope angle in terms of crack growth in the weak layer. Although similar mixed-mode criteria have been previously applied to other material systems

(Araki et al., 2005; Choupani, 2008; Jernkvist, 2001; Lim et al., 1994; Mall et al., 1983), this approach yielded limited statistical correlation with large interaction exponents.

Motivated by these facts, here we reexamine weak layer failure in the light of the well-established concept of brittle to plastic transition in structural mechanics. It is classically known that structural failure below a critical size is governed by material reaching its plastic strength rather than by crack propagation (Carpinteri, 1997). In fact, early studies toward development of PSTs report on a minimum slab length that is required for the measured critical cut length to remain independent of the slab length, a behavior which is characteristic of fracture-dominated failure (Gauthier and Jamieson, 2008b). Below such threshold, which as shown can easily reach larger than a meter in cases, the cut length varies in proportion with the slab length (Gauthier and Jamieson, 2008b), consistent with the classical theory of brittle-to-plastic transition (Carpinteri, 1997). This raises the question at what critical size such brittle to plastic transition happens for different slab-weak layer systems under mixed-mode loading conditions. Here, by analyzing the competition between classical fracture mechanics and plastic collapse, we demonstrate the existence of such transition as the characteristic size of the PST specimen decreases below a threshold, and how this threshold is affected by system parameters such as elastic properties of snow slab and weak layer, fracture toughness and plastic strength of the weak layer as well as the slope angle. There are indeed significant evidences in the literature regarding plastic/ductile behavior of snow in relation to the strain rate and temperature (Chandel et al., 2014b; Kirchner et al., 2001; Narita, 1980; Reiweger et al., 2015). While the prevailing interpretation of PSTs is largely based on mixed-mode fracture mechanics (Adam et al., 2024; Heierli et al., 2008; Sigrist et al., 2006), implicit in these analyses remains the assumption that the structural dimensions adopted based on general PST guidelines are large enough for fracture mechanics to dominate. Here, by showing that the extensive PST data reported by Adam et al. (2024) can more consistently be interpreted using a nonlinear plastic analysis based on a simple cap failure envelope model, we highlight the fact that original PST guidelines (Gauthier and Jamieson, 2008b) should be treated cautiously when applied to different snow slab-weak layer systems as plastic collapse may well persist to dominate even for conventional PST dimensions. The plastic analysis used here for the weak layer relies only on the normal plastic and shear strengths of a simple cap failure envelope for the weak layer. Variants of this failure model have already been invoked for weak layer characterization (Reiweger et al., 2015). Importantly, since the resulting formulation is remarkably simple and does not require knowledge of the poorly constrained mechanical properties of the overlying snow slab, it allows direct extraction of weak-layer plastic strengths from PST measurements. Within this framework, the propagation observed in conventional PSTs is not the advance of a brittle crack but rather the growth of a plastic zone, whereas crack-like propagation may emerge at larger scales—depending on material properties—such as those relevant to full-scale slab avalanches. Importantly, this framework generalizes naturally beyond classical weak-layer assumptions and extends to conditions such as wet snow, where material properties favor ductile behavior and are becoming increasingly relevant under climate change.

2. Modeling and Formulation

2.1 Fracture Mechanics failure

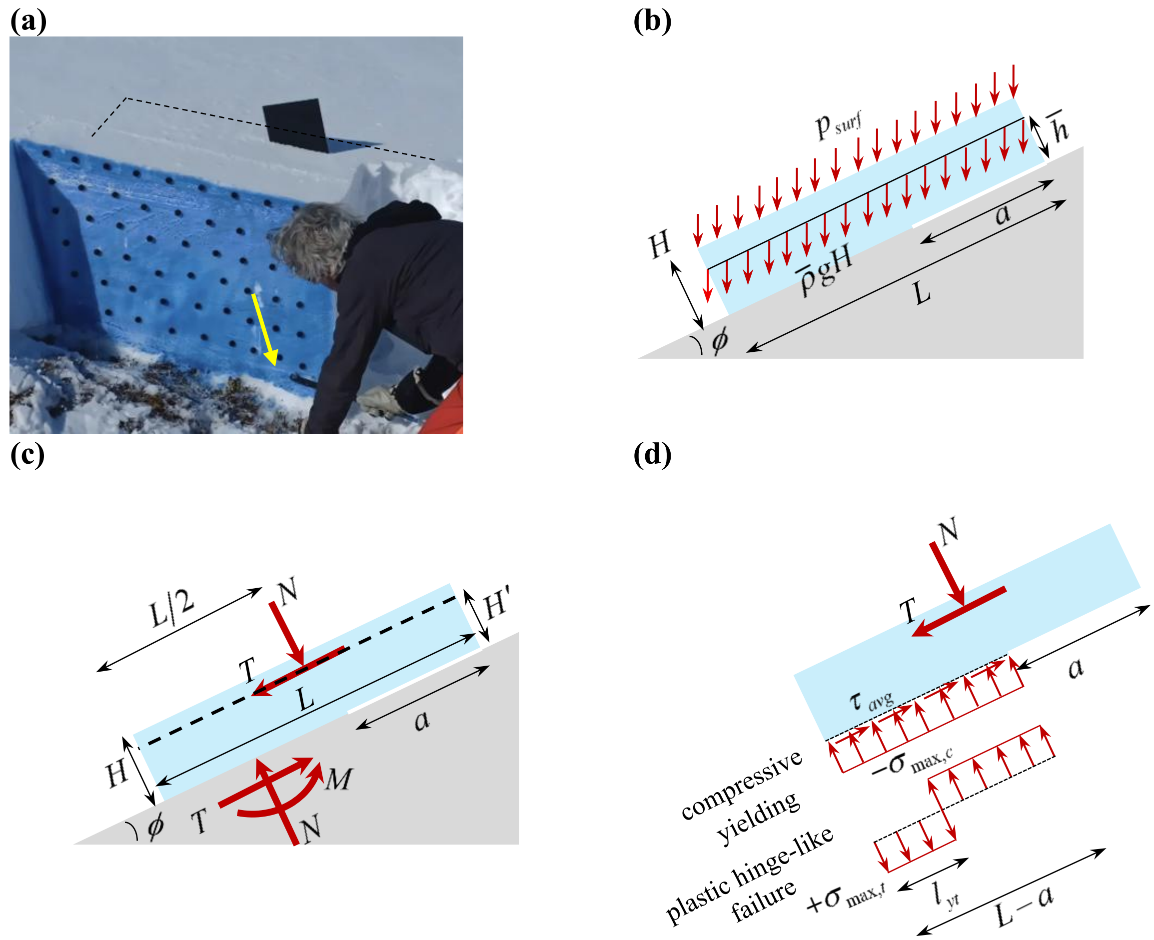

Fig. 1. (a) An isolated snow slab (outlined by the dashed lines) subject to PST by cutting upslope along the weak layer, marked by the yellow arrow (Fabio Gheser); (b) Schematics of a snow slab with a PST cut subject to a surface load p_{surf} as well as gravity, $\bar{\rho}gH$, $\bar{\rho}$ being mean density (of the slab above the weak layer), and g gravitational acceleration; (c) Equivalent loading system consisting of a tangential load T at distance H' from the weak layer, and a normal load, and N ; In addition to T and N , the bonded zone of the weak layer is subject to a moment M ; (d) Schematics of plastic collapse modes of a uniform compressive yielding and a plastic hinge-like failure at the weak layer; in the latter case l_{yc} is the interface length yielded in compression.

Consider a slab of snow of height H and length L resting on a weak layer on a slope of angle ϕ with an edge cut of length a created in a PST, as shown in Fig. 1 (b). Note that $\phi > 0$ corresponds to a downslope cut from the upper end of the slab, and $\phi < 0$ to an upslope cut at the lower end.

The slab is considered of an average density $\bar{\rho}$, subject to a vertical uniform surface load p_{surf} per unit length of the slab. A conventional way for modeling the snow slab on a weak layer is to invoke an elastic foundation model for the weak layer and consider the slab as an elastic beam. In the presence of a cut in a PST, both normal and tangential components (relative to the slope) of force and deformation are considered, and reactions of the elastic foundations are considered linearly proportional to the displacement components at the bottom of the slab, see Appendix A. Finding energy release rates of modes I (based on the anti-crack notion) and II, respectively denoted by G_I and G_{II}, one may utilize Griffith mixed mode fracture to predict the critical cut length. The conventional mixed-mode fracture criterion based on linear interaction between the two modes reads (Hutchinson and Suo, 1991)

$$\frac{G_I}{G_{Ic}}+\frac{G_{II}}{G_{IIc}}=1, \tag{1}$$

where G_{Ic} and G_{IIc} are the critical fracture energies of pure modes. To interpret their PST measurements of critical cut size vs. slope angle, as shown in Fig. 2(a), Adam et al. (2024) developed an elastic model which accounts for (i) shear-deformation of the beam, (ii) deformation variation across the weak layer thickness, and (iii) edge effects on loading. Their reported results together with the best fit found according to Eq. (1) are shown in Fig. 2(b), and the corresponding R^2 is given in Table I. One may argue that the material properties of the snow could vary from day to day. In this view, one is in principle left with the formidable task of adopting an elastic model, taking all material properties as fitting variables, and trying to find optimized model properties that could best match the experiments. While this is outside the scope of current work, it is relevant at least to allow different G_{Ic} and G_{IIc} values for measurements on different days, as done by Adam et al. (2024). Taking this approach, the resulting R^2 values based on day-to-day fitting are also included in Table I. The daily R^2 values reach 0.70 in just one case and remain below 0.3 in 6 out of all 9 cases.

While Eq. (1) is based on linear interaction of the two modes, Adam et al. (2024) examined several nonlinear interaction laws and proposed a phenomenological power-law modification of the type:

$$\left(\frac{G_I}{G_{Ic}}\right)^m + \left(\frac{G_{II}}{G_{IIc}}\right)^n = 1. \tag{2}$$

Combining this with the beam on elastic foundation model, they proposed $m = 5.0$ and $n = 2.2$. Their reported values of G_I and G_{II} normalized with respect to the respective critical values, together with Eq. (2) as fracture criterion are shown in Fig. 2(c). Applying transformation of variables and using linear regression for fitting Eq. (2) to their data, we computed the resulting R^2 as given in Table I both for fitting to all data and for day-to-day fitting.

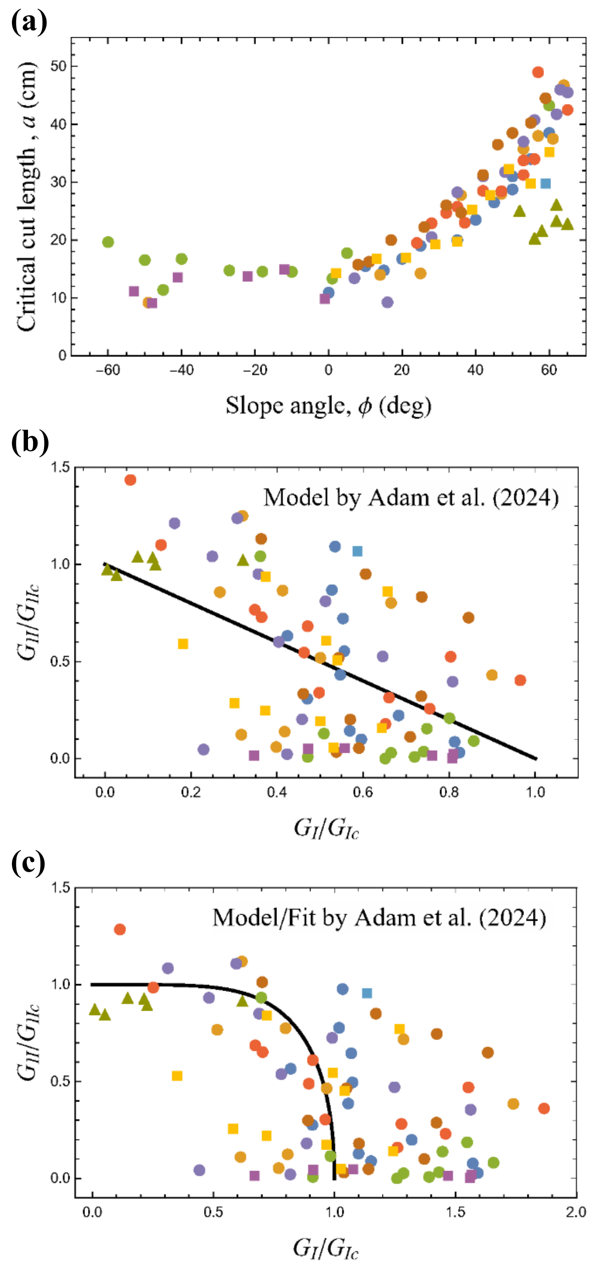

Fig. 2. (a) Experimental measurements of critical cut length vs. slope angle as reported by (Adam et al., 2024) and predictions of the plastic collapse model for three different loadings: a clear trend is emerging; (b) Plot of G_{II}/G_{IIc} vs. G_I/G_{Ic} for the reported energy release rate calculations of (Adam et al., 2024) as fitted to a linear mixed mode criterion, Eq. (1), using single values of G_{Ic} and G_{IIc}: the clear trend is lost; (c) Similar plot as in (b) with the nonlinear interaction law, Eq. (2) , proposed by (Adam et al., 2024) for fitting: the clear trend is lost. The black solid lines in (b) and (c) show the interaction laws used. Different colors have been used for tests on different days, and different symbols, indicate tests with different surface loads, circles, squares, and triangles, respectively for $p_{surf} = 1.59\,\mathrm{kN/m^2}$, $1.48\,\mathrm{kN/m^2}$, and $2.53\,\mathrm{kN/m^2}$.

Further trying to understand the test data of Adam et al. (2024) based on the fracture mechanics approach, we applied the theoretical models of Appendix A, based on coupled Euler-Bernoulli (EB) or Timoshenko beam models of the slab resting on an elastic foundation, to their experimental conditions and used Eq. (1) with G_{Ic} and G_{IIc} as the fitting variable. The results together with the failure criterion Eq. (1) are shown in Fig. 3(a) and (b). Results shown have been found by consistently considering $\bar{\rho} = 200\,\mathrm{kg/m^3}$, $H = 11.5$ cm, $L = 1\,\mathrm{m}$, with variable surface loads of $p_{surf} = 1.59\,\mathrm{kN/m^2}$, $1.48\,\mathrm{kN/m^2}$, and $2.53\,\mathrm{kN/m^2}$ applied in different experiments. The Young's moduli of the slab and weak layer are respectively taken as $E = 30\,\mathrm{MPa}$, and $E_{wl} = 0.15\,\mathrm{MPa}$, with a Poisson's ratio of $\nu = 0.25$ for both, and a 2 cm-thick weak layer (Adam et al., 2024). The corresponding R^2 value is 0.14, which with the exclusion of a single data point far from similar measurements on the same day, improves to 0.21, see Table I (in this table, the numbers shown in parentheses in the sublines are those found by exclusion of this single off-trend data point). The resulting R^2 values based on day-by-day fitting are also included in Table I for the EB theory, and those found from Timoshenko beam theory remain within ± 0.02 of the EB theory. Disregarding one data point from the data, R^2 reaches 0.6 and larger only for tests on two days, remaining below 0.2 for tests on 5 out of 9 days. These results confirm those by Adam et al. (2024), reported in Fig. 2(b) and (c).

All the above calculations rely on a certain set of numerical values for the material properties of the snow and weak layer. Given the level of uncertainty, we also examined a special case of elastic models where the slab is significantly stiff compared to the weak layer, which is of particular interest as it can not only be treated analytically but also does not require assumptions regarding numerical values of the material properties. Details of the model are given Appendix B. Applying this model to the data set of (Adam et al., 2024) with Eq. (1) as the fracture criterion, the results are shown in Fig. 3(c), and the R^2 values are included in Table I. Interestingly, among elastic models, the latter model which treats the slab as to be rigid and thus accounts only for elasticity of the weak layer provides the best predictions for all as well as for day-to-day measurements except for one day, i.e. Mar 09 tests.

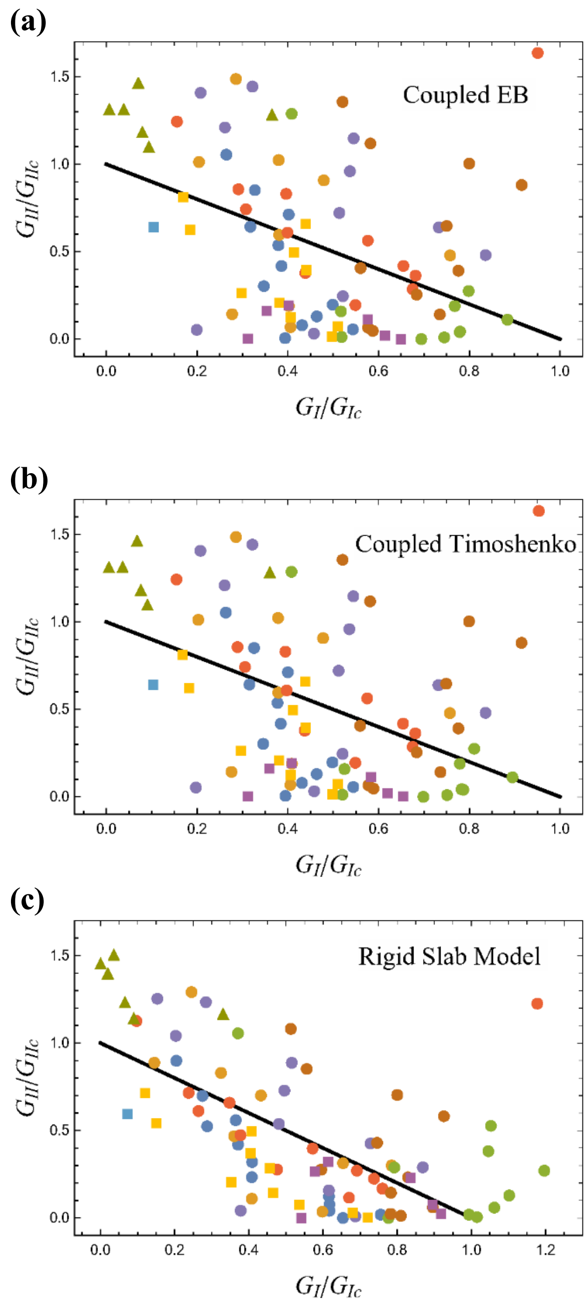

Fig. 3. Plots of normalized energy release rates, G_{II}/G_{IIc} vs. G_I/G_{Ic}, calculated according to different models using single values of G_{Ic} and G_{IIc} for fitting to the linear interaction law, Eq. (1) shown by the solid black line: (a) Coupled Euler-Bernoulli beam model, (b) coupled Timoshenko beam model, see Appendix A for both models, and (c) the rigid slab model, Appendix B. The fits shown are based on the elimination of one data point in red which falls significantly off-trend.

2.2. Evidence of plastic collapse

Since various efforts based on elastic models combined with fracture mechanics criteria do not appear to us to provide a satisfactory explanation for the experiments, here we treat the problem from the different viewpoint of plastic failure in the weak layer. This is in particular relevant as it is known that a transition from brittle to plastic failure arises when structural dimensions fall below a threshold (Carpinteri, 1997), and that snow is indeed capable of exhibiting ductile deformation under suitable loading/environmental conditions both under tension and compression (Chandel et al., 2014b; Narita, 1980; Reiweger et al., 2015). In the following, relying on static equilibrium considerations, we present a simple nonlinear plastic failure analysis in the weak layer. With the exception of the normal and shear strengths of the cap failure envelope treated as fitting parameters, the analysis does not require assumptions regarding material properties of the snow and weak layer.

Let $N = W\cos\phi$ and $T = W\sin\phi$ represent the normal and tangential components of the overall load on the slab, $W = (p_{surf} + \bar{\rho}gH)L$ being the total vertical load (per unit width of the slab normal to the plane) including the surface load and the slab weight $\bar{\rho}gH$, $\bar{\rho}$ the average slab density (above the weak layer), and g the gravitational acceleration. The tangential load is assumed effectively applied at a distance H' from the weak layer as shown in Fig. 1(c) to accommodate the fact that the center of mass of the slab and the applied surface load are at different heights. Hence, $H' = \frac{p_{surf}H + \bar{\rho}gH\bar{h}}{p_{surf} + \bar{\rho}gH}$, where $\bar{h}$ is the distance between the center of mass of the slab and the weak layer, Fig. 1(b), e.g. $\bar{h} = H/2$ for a homogeneous slab, and $H' \approx H$ for $p_{surf} \gg \bar{\rho}gH$. Equilibrium of the slab implies that the bonded zone of the weak layer in addition to the normal force N considered at its center, and shear force T, is subject to the moment:

$$M = N\left(\frac{L}{2}\right) - N\left(\frac{L-a}{2}\right) - TH' = \frac{Na}{2} - TH', \tag{3}$$

as both normal and tangential components of the loading and weak layer reactions are not colinear, see Fig. 1(c).

Let $\sigma_{\max,c}$ denote the normal compressive yield stress of the weak layer when it is simultaneously subject to the average shear stress $\tau_{avg} = \dfrac{W\sin\phi}{L-a}$. A simple cap failure envelope reads:

$$\sigma_{\max,c}^2 + \beta_p \tau_{avg}^2 = Y^2 \text{, or equivalently, } \left(\frac{\sigma_{\max,c}}{\sigma_{cr}}\right)^2 + \left(\frac{\tau_{avg}}{\tau_{cr}}\right)^2 = 1, \tag{4}$$

where β_p, Y, σ_{cr}, and τ_{cr} are material constants related through $\sigma_{cr} = \tau_{cr}\sqrt{\beta_p} = Y$. The maximum tensile yield stress $\sigma_{\max,t}$ in the presence of the shear stress τ_{avg} can in general be considered a fraction of the compressive yield stress as $\sigma_{\max,t} = \alpha\sigma_{\max,c}$, α being a constant. It should be noted here that although Eq. (4) suggests τ_{cr} as the shear plastic strength of the weak layer in the absence of the compressive stress, i.e. for $\sigma_{\max,c} = 0$, however, the cap model is known to overestimate the shear stress that the material can sustain at low pressures, and hance is in practice often replaced with a different envelope such as the Mohr-Coulomb failure envelope, as already demonstrated for snow (Reiweger et al., 2015), see also Section 2.4. In this sense, τ_{cr} is an effective shear plastic strength predicted by the cap model within the fitted experiments, and not the true shear strength of the material thus measured under zero/negligible compressive stress. However, as it will be shown in the following, the cap part of the failure envelope largely suffices for interpretation of the PST results as the compressive stresses in these tests remain significant for the range of the tested slope angles.

Subject to a combination of the compressive force N and the moment M, weak layer failure in general arises by yielding in tension over a length l_{yt}, and in compression over the remaining length $L-a-l_{yt}$ as shown in Fig. 1(d), corresponding to a plastic hinge-like failure. The normal force and moment equilibrium equations read:

$$\sigma_{\max,c}\left((L-a)-(1+\alpha)l_{yt}\right) = W\cos\phi, \tag{5}$$

$$\frac{\sigma_{\max,c}}{2}\left((L-a)^2-(1+\alpha)l_{yt}^2\right) = W\left(\cos\phi\frac{L}{2}-\sin\phi H'\right). \tag{6}$$

For an experimentally measured set of values of ϕ and a under a given load W corresponding to failure in a PST, Eqs. (5) and (6) can be solved for l_{yt} and $\sigma_{\max,c}$ which can be cast in the following dimensionless form:

$$\frac{l_{yt}}{L} = \varepsilon - \sqrt{\varepsilon^2 + \frac{1}{(1+\alpha)}\left(1-\frac{a}{L}\right)\left(1-\frac{a}{L}-2\varepsilon\right)}, \tag{7}$$

$$\frac{\sigma_{\max,c} L}{W_{ref}} = \frac{W}{W_{ref}} \cos\phi \left(1-\frac{a}{L}-(1+\alpha)\frac{l_{yt}}{L}\right)^{-1}, \tag{8}$$

where $\varepsilon = \frac{1}{2} - \tan\phi \frac{H'}{L}$, and W_{ref} is an arbitrary reference load introduced for normalization purposes. Since only solutions with $l_{yt} \geq 0$ are physically admissible, the limiting case of $l_{yt} = 0$ is enforced when a negative solution for l_{yt} follows from Eq. (7), corresponding to the scenario of uniform yielding of the weak layer under compression, see Fig. 1(d). The calculated values of $\frac{\sigma_{\max,c} L}{W_{ref}}$ and $\frac{\tau_{avg} L}{W_{ref}} = \frac{W \sin\phi}{W_{ref}}$ based on the experimental data of (Adam et al., 2024) are then fitted to the failure criterion, Eq. (4). To this end, we treat $\left(\sigma_{\max,c} L / W_{ref}\right)^2$ and $\left(\tau_{avg} L / W_{ref}\right)^2$ respectively as the dependent and independent variables, which allows us to use a linear regression scheme with $\sigma_{cr}^2 = Y^2$ and $\beta_p = \left(Y/\tau_{cr}\right)^2$ as fitting parameters. Note that inverting the procedure would provide slightly different best-fitting values especially for the last parameter that is indeed effective, since these experiments always present significant normal loads (this difference is thus not significant here but could be removed by minimizing the experimental points distance from the theoretical cap thus renouncing to the two possible linear regressions). Here, we use $\alpha = 1$ for further simplicity and reducing the best fitting parameters. Fig. 4(a) shows the computed values of $\frac{\sigma_{\max,c}}{\sigma_{cr}}$ vs. $\frac{\tau_{avg}}{\tau_{cr}}$ which have been found (ρ, H, L, p_{surf} same as before). The resulting values for the fitting parameters are $\sigma_{cr} = Y = 2.31\text{kPa}$ and $\tau_{cr} = 1.85\sigma_{cr}$ with $R^2 = 0.38$ based on 88 data points, which correspond to all experiments performed on 10 different days, see the first rows of Tables I (plastic model) and II. Elimination of one off-trend data point, evident in Fig. 3(b), improves R^2 to 0.47, corresponding to $\sigma_{cr} = Y = 2.32\,\text{kPa}$ and $\tau_{cr} = 1.76\sigma_{cr}$, see the subline of the first row in Tables I (plastic model) and II. We note that the critical stresses found are comparable with the range reported by Reiweger et al. (2015), reaching as high as 2.6 kPa and 5.7 kPa depending on the loading rate.

Allowing material properties to vary on different days, as absolutely naturally expected for snow, fitting results are shown in Fig. 4(b), and the corresponding material parameters found are given in Table II. In the figure, open markers have been used for the cases where uniform compressive yielding is dominant, and filled markers correspond to the plastic hinge-like failure (Fig. 1(d)). The respective R^2 values for the daily fits are listed in Table I. With the exclusion of one data point, which belongs to tests on Feb 25, R^2 values for tests on individual days vary between 0.60 and 0.92 for tests on all 9 days, exhibiting significant improvement over other models in Table II.

Note that all the results shown in Fig. 4(a) and (b) remain within the range of $\sigma_{\max,c}$ larger than $\approx 0.4\sigma_c$. Hence our analysis rests only on the applicability of the cap failure envelope within this range and does not preclude the possibility of a Mohr-Coulomb failure envelope to dominate when the compressive stress is lower than ~40% of the compressive plastic strength. In this sense, the presented values of τ_{cr} based on the cap model are effective and expected to overestimate the true shear strength of the weak layer. This is consistent with our fitting values providing plausible normal plastic (not peak) strength of the order of a couple of kPa and a ratio between plastic effective shear and normal strengths of ~1.85. Note that this ratio reduces to ~1.14 if we use a linear regression exchanging dependent and independent variables. This last ratio of ~1.14 is incidentally very close to that reported in (Chandel et al., 2014a) where a cap failure envelope was fitted to independent normal or tangential snow experiments, showing a good correlation. In general, a Mohr-Coulomb failure envelope should be considered at low normal stress as already demonstrated for snow (Reiweger et al., 2015).

Using values of model parameters found from fitting, one may go back to find variations in the critical cut length vs. slope angle. Results are included in Fig. 4(c) for the three surface loads: the black solid line for the tests represented by circles, and the upper and lower dashed lines for those shown by the squares and triangles, respectively. These results have been found by taking Y and β_p to be average of their daily values found from fitting for days on which tests were performed under identical surface loading. An interesting observation here is that while the critical cut length exhibits a clearly increasing trend vs. slope angle for $\phi > 0$, i.e. downslope cuts from the upper edge, the trend appears to be somewhat mixed within $\phi < 0$, corresponding to an upslope cutting direction from the lower slab edge. It is remarkable that similar to the model (Heierli et al., 2008), the present plastic failure model identifies normal deformation as a critical factor to failure. The fact that the current theory predicts mixed trends for upslope cuts is also noteworthy in view of the observations which suggest contradictory trends (Bergfeld et al., 2025), which is even apparent in the controlled experiments of Adam et al. (2024), see Fig. 2(a) for $\phi < 0$. However, the most important conclusion is that plastic collapse of the weak layer can persist to dominate even for the dimensions of the conventional PSTs. This result also hints at the lack of universal applicability of the existing guidelines for performing such tests, as fracture-dominant regime may require slabs longer than previously thought, i.e. typically around one meter, depending on a number of factors as will be shown in the following section.

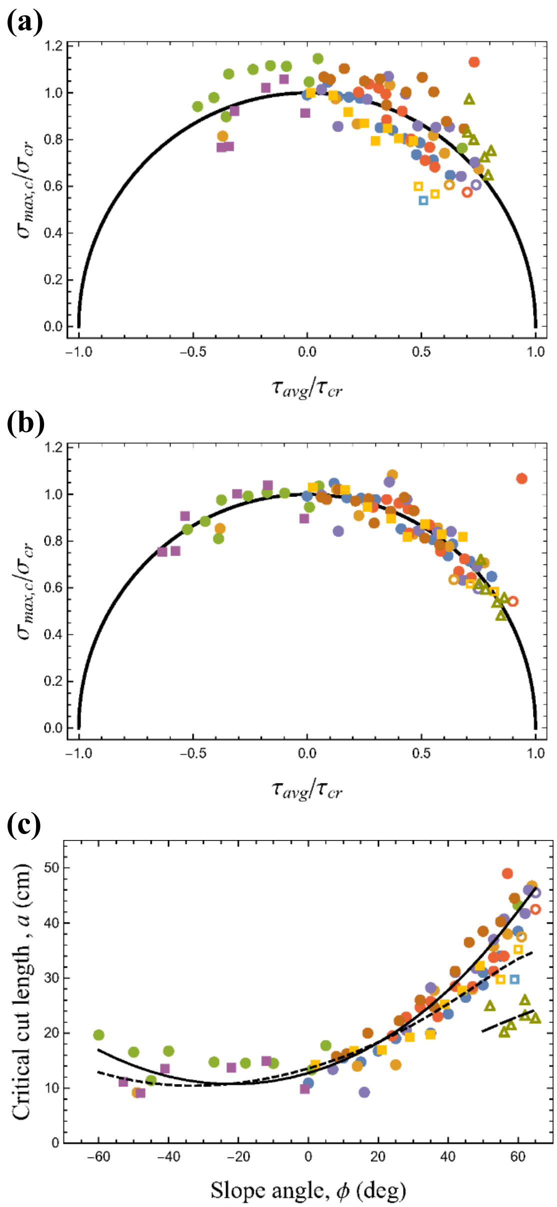

Fig. 4. (a) Plot of $\sigma_{\max,c}/\sigma_{cr}$ vs. τ_{avg}/τ_{cr} based on fitted values of $\sigma_{cr}=Y$ and τ_{cr} according to Eq. (4) for the critical cut length vs. slope angle data of (Adam et al., 2024) using Eqs. (7) and (8) ; (b) Same results as in (a) but normalized with respect to the day-to-day material properties obtained by fitting as given in Table I, with the corresponding R^2 values in Table I; (c) Predictions of the plastic collapse model for critical cut length vs. slope angle and experimental measurements of (Adam et al., 2024) for three different loadings. Filled or open markers indicate plastic hinge-like or uniform compressive failures, respectively. Different symbols, i.e. circles, squares and triangles, are respectively for $p_{surf}=1.59\,\mathrm{kN/m^2}$, $1.48\,\mathrm{kN/m^2}$, and $2.53\,\mathrm{kN/m^2}$. Respective predictions of the plastic model are shown by the solid line, and the upper and lower dashed lines in (c), using the average values of the parameters, Y, β, found from daily fits for days on which tests were performed under the same loading.

Table I. Comparison of R^2 for different models: the best fit is found for the present plastic model.

	Number of tests	Elastic-slab fracture models			Rigid slab model & Eq. (1)	Plastic weak layer model
		Elastic model* & Eq. (1)	Elastic model* & Eq. (2)	EB beam on elastic foundation & Eq. (1)		
All data	88 (87)	0.29	0.11	0.14 (0.21)	0.38 (0.49)	0.38 (0.47)
1 (Feb 18)	12	0.37	0.17	0.60	0.88	0.92
2 (Feb 23)	9	0.01	0.04	0.06	0.50	0.61
3 (Feb 24)	10	0.33	0.16	0.35	0.40	0.79
4 (Feb 25)	12 (11)	0.70	0.12	0.00 (0.74)	0.01 (0.86)	0.10 (0.87)
5 (Mar 02)	11	0.14	0.12	0.07	0.51	0.69
6 (Mar 03)	11	0.01	0.00	0.00	0.35	0.66
7 (Mar 07)	1					
8 (Mar 08)	10	0.01	0.01	0.45	0.81	0.88
9 (Mar 09)	6	0.20	0.38	0.16	0.10	0.64
10 (Mar 10)	6	0.26*	0.07	0.01	0.43	0.60

*Energy release rates based on calculations of (Adam et al., 2024).

†The number in parentheses in the subline of this row, and also for Feb 25, are based on elimination of a single data point form the latter data set which appeared to be significantly off-trend, see Figs. 3 and 4, and whose elimination in some models led to significant improvement of R^2, e.g. from 0.10 to 0.87 in Feb 25 data.

Table II. Numerical values of the model parameters used for fitting to tests on all data as well as on day-to-day data as shown in Fig. 2(b).

	$\sigma_{cr} = Y$ (kPa)	τ_{cr}/σ_{cr}
All data	2.31 (2.32)	1.85 (1.76)
Feb. 18	2.32	1.36
Feb. 23	2.22	1.79
Feb. 24	2.57	1.45
Feb. 25	2.24 (2.46)	2.32 (1.29)
Mar. 02	2.36	1.71
Mar. 03	2.50	1.93
Mar. 08	2.25	1.24
Mar. 09	2.36	1.02
Mar. 10*	3.13	1.22

*Extra load applied in the experiments.

2.3. Plastic to brittle transition: from PST to real avalanches

The analysis above indicates that a simple although nonlinear plastic analysis based on a cap failure envelope provides a much better explanation for the experimental measurements of standard (1 m) PST when compared to fracture mechanics-based criteria. This raises the question regarding how structural dimensions in combination with material properties regulate a transition from one failure mode to another.

To address this question, we developed an analytically tractable model in which the beam is subject to uniformly distributed tangential and normal loads γ_t and γ_n as well as a uniformly distributed moment $\gamma_t e$, $e = H' - 0.5H$ being eccentricity of the tangential load relative to the slab midplane, see Appendix C. Further, the beam segment over the bonded zone of the weak layer is considered subject to an additional distributed moment $\dfrac{\gamma_t LH}{2(L-a)}$, accounting in an average sense for the moment generated by the shear reaction of the elastic foundation. The model allows analytical calculation of the energy release rate as:

$$G = \frac{\gamma_n^2}{2k_n} g_I\left(\frac{a}{L}, \lambda_n L; \phi, \eta_1, \frac{H}{L}\right) + \frac{\gamma_t^2}{2k_t} g_{II}\left(\frac{a}{L}, \lambda_t L\right), \tag{9}$$

where $g_I\left(\frac{a}{L},\lambda_n L;\phi,\eta_1,\frac{H}{L}\right)$ and $g_{II}\left(\frac{a}{L},\lambda_t L\right)$ are dimensionless expressions given in Appendix C, $\lambda_n=\left(\frac{(1-\nu^2)k_n}{4E\bar{I}}\right)^{1/4}$, $\lambda_t=\left(\frac{(1-\nu^2)k_t}{EH}\right)^{1/2}$, and $\eta_1=\frac{e}{L}$. Here, k_n and k_t are respectively the elastic foundation stiffness constants in the normal and tangential directions relative to the slope, with E and ν respectively the elastic modulus and Poisson's ratio of the slab, and $\bar{I}$ the second moment of the slab's cross-section per unit width, e.g. $\bar{I}=\frac{1}{12}H^3$ for a homogeneous slab.

Letting $\gamma_n=\frac{W\cos\phi}{L}$, $\gamma_t=\frac{W\sin\phi}{L}$ and imposing the Griffith criterion $G=G_c$ for crack growth, G_c being the fracture energy (per unit area), the critical load of fracture W_{cf} can be found from Eq. (9) and cast in the dimensionless form of:

$$\frac{W_{cf}}{LY}=\frac{\left(2G_c k_n\right)^{1/2}}{Y}\left[\cos^2\phi g_I\left(\frac{a}{L},\lambda_n L;\phi,\eta_1,\frac{H}{L}\right)+\frac{k_n}{k_t}\sin^2\phi g_{II}\left(\frac{a}{L},\lambda_t L\right)\right]^{-1/2}. \tag{10}$$

Note the emergence of a characteristic fracture stress $\sigma_{cf}=\sqrt{2k_n G_c}$.

While Eq. (10) governs fracture-driven collapse, the critical load of plastic failure W_{cp} can be found from Eq. (4) upon insertion of Eq. (8), and solving the resulting equation for W as:

$$\frac{W_{cp}}{LY}=\left(\cos^2\phi\left(1-\frac{a}{L}-(1+\alpha)\frac{l_{yt}}{L}\right)^{-2}+\beta_p\sin^2\phi\left(1-\frac{a}{L}\right)^{-2}\right)^{-\frac{1}{2}}. \tag{11}$$

For a given ϕ, $\eta=\frac{H'}{L}$, and $\frac{a}{L}$, the dimensionless critical load of Eq. (11) depends only on β_p for the plastic failure, and that of Eq. (10) depends on $\frac{\sigma_{cf}}{Y}$, $\lambda_t L$, $\lambda_n L$, $\frac{k_n}{k_t}$, and $\frac{H}{L}$ for brittle fracture ($\eta_1=\eta-\frac{H}{2L}$). For different slope angles, Fig. 5 shows variations in dimensionless critical loads as a function of the relative cut size a/L for several values of the normalized slab length $\lambda_n L$. Plastic collapse loads are for choices of β_p as shown in the figure, and results of brittle fracture are for $\lambda_n = 4\lambda_t$, $\eta = 2\eta_1 = 0.2$, $\sigma_{cf} = 2Y$, and $\nu = 0.25$ (for both weak layer and the slab). Note that $\frac{k_n}{k_t} = \frac{2}{1-\nu}$, and $\frac{\lambda_n}{\lambda_t} = \left(\frac{12 t_{wl}}{(1-\nu)^2 H} \frac{E}{E_{wl}} \right)^{1/4}$ based on elastic foundation constants of $k_n = \frac{E_{wl}}{t_{wl}(1-\nu^2)}$, $k_t = \frac{E_{wl}}{2t_{wl}(1+\nu)}$, for $\bar{I} = \frac{H^3}{12}$ (homogeneous slab), with E_{wl} and t_{wl} respectively elastic modulus and thickness of the weak layer. For comparison, the solution derived in Appendix B based on fracture mechanics for a rigid slab corresponding to the limit of $\lambda_n \to 0$ is also included in the figure. The curves shown suggest that plastic failure becomes dominant over the brittle mode with decreasing the dimensionless slab length $\lambda_n L$ at a given a/L. Note that a small enough $\lambda_n L$ for the onset of plastic transition is also equivalent to a large enough slab thickness as λ_n for a homogeneous slab scales as $H^{-3/4}$. A noteworthy observation is that at a fixed critical load, $W_{cr}/(LY)$, the plastic curves for a given β_p predict a constant a/L, implying that the critical cut length scales with slab dimension within the plastic collapse regime. In comparison, within the brittle regime, the value of a/L reduces with increasing slab length at a fixed $W_{cr}/(LY)$, i.e. with increasing $\lambda_n L$ (keeping all other parameters unchanged), suggesting that a constant cut length is eventually approached for long enough slabs, consistent with classical fracture mechanics predictions. Gauthier and Jamieson (2008b) based on experimental observation of such a transition, which in some cases they found to happen at slab lengths even longer than 1 m, provided guidelines to avoid the plastic collapse regime. However, these guidelines appear not to be universally applicable as revealed by the analysis of the tests results reported by Adam et al. (2024) in the preceding section. Fig. 5(f) shows variation with σ_{cf}/Y in the dimensionless critical size $\lambda_n L_c$ below which plastic collapse becomes fully dominant for all crack sizes. Although the exact threshold size for transition depends on a number of factors, estimates of the dimensionless size $\lambda_n L$ are of interest. For $E = 30\,\text{MPa}$, $E_{wl} = 0.15\,\text{MPa}$, $\nu = \nu_{wl}$, typical slab dimensions of $H = 0.4\,\text{m}$, $L = 1\,\text{m}$, and a weak layer thickness of $t_{wl} = 2\,\text{cm}$, one arrives at $\lambda_n L = 1.82$. Keeping all other parameters fixed, $\lambda_n L$ changes to 3.11 for $H = 0.2\,\text{m}$, to 1.36 for $E = 100\,\text{MPa}$, and to 2.62 for $t_{wl} = 0.5$ cm. These estimates suggest that the transition illustrated in Fig. 5 is highly relevant for the typical slab length of ~1 m in PSTs and thus confirms that plastic collapse can be predominant at the size scales of a few meters. We thus suggest long and not standard PST for measuring the fracture properties of snow relevant to the real size-scale of avalanches.

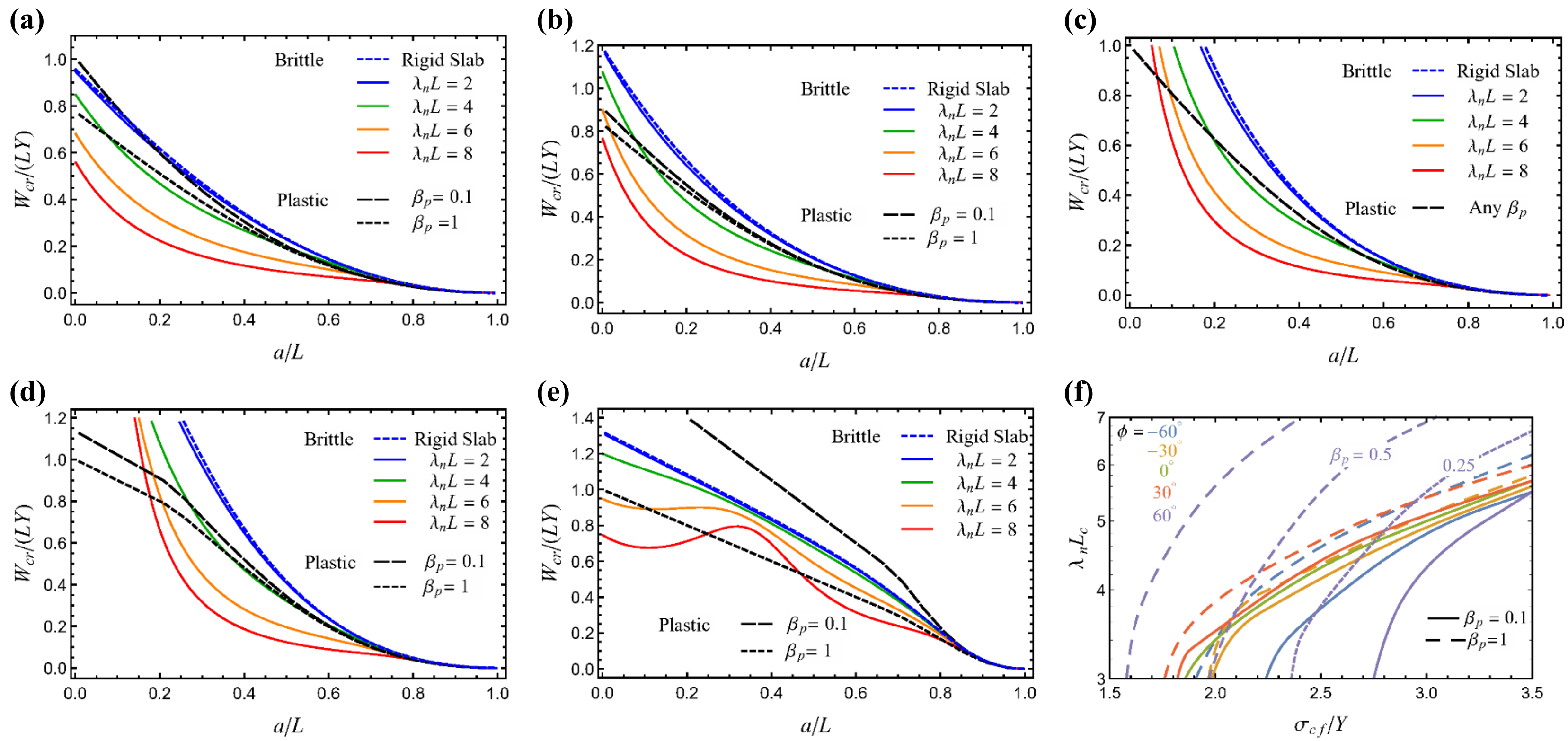

Fig. 5. Normalized critical load of failure W_{cr} based on brittle fracture and plastic collapse for slope angles of (a) $\phi = -60^\circ$, (b) $\phi = -30^\circ$, (c) $\phi = 0^\circ$, (d) $\phi = +30^\circ$, and (e) $\phi = +60^\circ$; Results shown are for $\lambda_t = \lambda_n/4$, $\sigma_{cf} = 2Y$, $\eta = 2\eta_1 = 0.2$, $\nu = 0.25$, with results of the rigid slab model, i.e. $\lambda_n L \to 0$, also included, see Appendix B; (f) Dimensionless critical size below which plastic failure becomes dominant for any crack size as a function of σ_{cf}/Y keeping other parameters the same as before (the curve for $\phi = 0^\circ$ is for any β_p).

2.4. Interpretation of the results

As noted in the previous section, transition from plastic collapse to brittle fracture arises when the length of the PST slab exceeds a certain critical size. Hence, although the nonlinear analysis based on plastic collapse predicts a constant a/L at a fixed $W_{cr}/(LY)$, this result is not applicable to PSTs performed on long enough slabs (Bergfeld et al., 2023) where brittle fracture is predicted to dominate as shown by the transition theory above. In fact, fracture mechanics principles together with elastic analysis remain crucial for analysis of such cases in predicting the critical cut length. The analysis above rather suggests that the transition length can readily exceed around one meter, typical to conventional PSTs, hence calling into question applicability of fracture mechanics for conventional PST dimensions. Our analysis, hence, should not be interpreted as if the critical cut length keeps increasing with the slab dimension indefinitely. Rather, this is only the case below a critical length which could be found experimentally by testing slabs of variable lengths under otherwise similar conditions, including slope, loading and slab thickness. This is also consistent with early reports on PSTs (Gauthier and Jamieson, 2008b). An alternative interpretation of our results is that below the transition size, the fracture process zone, also known as the cohesive zone, can grow all the way to encompass the entire length of the slab. In this regard, one may note that estimates of the cohesive zone size can become comparable to, and even exceed, the slab length of 1 m (McClung and Schweizer, 2006).

Further, one should note that the analysis here presents a simple interpretation of the PST results in terms of a simple cap failure envelope of the type $\left(\sigma/\sigma_{cr}\right)^2+\left(\tau/\tau_{cr}\right)^2=1$. This allowed us to estimate numerical values for the critical normal and shear stresses, σ_{cr} and τ_{cr} of the cap model based on PST measurements. However, it should be cautioned that these values have been extracted based on PST results which in the case of (Adam et al., 2024) have been performed for slopes below 65°, and as a result the weak layer is always subject to some normal compressive stress. In fact, our analysis relies on the cap model only within σ larger than $\approx 0.4\sigma_{cr}$, see Fig. 4(a) and (b). Naturally, PST does not provide information regarding failure envelope behavior at low compressive stresses as the tested slopes remain well below 90° ideally required for a zero normal stress on the weak layer. This observation is crucial since it is widely found that, at the low-compressive-stress regime, behavior of the material could be dominated by a different failure envelope, the most well-known of them being the linear Mohr-Coulomb criterion, see e.g. (Reiweger et al., 2015). The behavior that the shear strength falls as the normal compressive stress σ approaches near zero values has been found experimentally (Chandel et al., 2014a; Jamieson and Johnston, 1998; McClung, 1977; Nakamura et al., 2010; Perla et al., 1982; Reiweger et al., 2015), and further confirmed by numerical simulations (Blatny et al., 2021; Bobillier et al., 2020; Chandel et al., 2015; Mede et al., 2018). Hence, one should avoid the pitfall of interpreting the numerical values of τ_{cr} found here based on the cap model as the shear strength of the material. Recently Schöttner et al. (2026) have measured strength of weak layers under mixed loading and used cap model to extract σ_{cr} and τ_{cr} of the weak layer. They found that τ_{cr} remains below $\approx 0.71\sigma_{cr}$. Unfortunately, due to significant scatter in their measurements, it remains unclear if the cap model really governs the entire range of strength variations reported. In contrast, measurements by Chandel et al. (2014a) in several cases reveal that the failure envelope follows a cap model. It is of interest that in one case they find the cap model parameter τ_{cr} to be $\approx 1.23\sigma_{cr}$. A further point worth considering is that the ratio of τ_{cr}/σ_{cr} found here from fitting to a cap model could also vary with the fitting scheme used. For example, using a linear regression scheme treating τ_{avg}^2 as the dependent variable as a function of $\sigma_{\max}^2$ treated as the independent variable, instead of doing the opposite, reduces the ratio of τ_{cr}/σ_{cr} from 1.85 reported above to 1.14 and also increases σ_{cr} to $2.63\,\text{kPa}$, without changing R^2. Indeed, performing strength measurements along with PST measurements similar to (Adam et al., 2024) for the same specimens remains an independent way of verifying the values of σ_{cr} and τ_{cr} found here, and could further shed light on the extent of applicability of the cap model. Such a coupled study is however lacking at this point.

3. Conclusion

Variants of elastic models/fracture criteria cannot adequately explain conventional PST results. In particular, while critical cut length vs. slope measurements show a nearly clear trend, the computed energy release rates for the two modes exhibit weak correlation. Since it is well-established that structural failure below a critical size is governed by plastic collapse rather than brittle fracture, we hypothesized that plastic collapse could still govern weak layer behavior in the dimensions of the conventional PSTs. It was shown that a nonlinear plastic analysis based on a simple cap failure envelope used in combination with basic static equilibrium conditions can explain extensive standard PST results performed for various slope angles for both upslope and downslope cuts under different loadings. The cap failure model relies only on two parameters, i.e. the normal and shear plastic strengths of the weak layer. An analytical model was developed to demonstrate the plastic-to-brittle transition and to examine how elastic properties of snow and weak layer, fracture toughness and plastic strength of the weak layer as well as the slope angle influence the onset of this transition, from standard (1 m) PST to real avalanches. Our results are consistent with PST observations suggesting that the critical cut length scales with slab length below a threshold which could reach larger than a meter. The results additionally suggest that plastic collapse could persist to dominate even for standard PST dimensions adopted according to general guidelines and thus suggest longer PST for addressing the fracture properties relevant to avalanches. Importantly, the presented framework generalizes beyond classical weak-layer assumptions to the wet snow conditions where ductile behavior is promoted by global warming.

Acknowledgements

The authors acknowledge funding from the European Research Council (ERC) under the European Union's Horizon Europe research and innovation program (ERC-AdG-2024 FRAMEGLOW "Advanced quantized FRActure MEchanics models of ice and snow for GLObal Warming risk mitigation," Grant Agreement No. 101201568, PI Nicola M. Pugno).

Declaration of interests

The authors declare no competing interests.

References

Adam, V., Bergfeld, B., Weißgraeber, P., van Herwijnen, A., Rosendahl, P.L., 2024. Fracture toughness of mixed-mode anticracks in highly porous materials. Nat. Commun. 15, 7379.

Araki, W., Nemoto, K., Adachi, T., Yamaji, A., 2005. Fracture toughness for mixed mode I/II of epoxy resin. Acta Mater. 53, 869–875. https://doi.org/10.1016/j.actamat.2004.10.035

Benzeggagh, M.L., Kenane, M., 1996. Measurement of mixed-mode delamination fracture toughness of unidirectional glass/epoxy composites with mixed-mode bending apparatus. Compos. Sci. Technol. 56, 439–449. https://doi.org/10.1016/0266-3538(96)00005-X

Bergfeld, B., Birkeland, K.W., Adam, V., Rosendahl, P.L., van Herwijnen, A., 2025. The effect of propagation saw test geometries on critical cut length. Nat. Hazards Earth Syst. Sci. 25, 321–334. https://doi.org/10.5194/nhess-25-321-2025

Bergfeld, B., van Herwijnen, A., Bobillier, G., Rosendahl, P.L., Weißgraeber, P., Adam, V., Dual, J., Schweizer, J., 2023. Temporal evolution of crack propagation characteristics in a weak snowpack layer: conditions of crack arrest and sustained propagation. Nat. Hazards Earth Syst. Sci. 23, 293–315. https://doi.org/10.5194/nhess-23-293-2023

Blatny, L., Löwe, H., Wang, S., Gaume, J., 2021. Computational micromechanics of porous brittle solids. Comput. Geotech. 140, 104284. https://doi.org/10.1016/j.compgeo.2021.104284

Bobillier, G., Bergfeld, B., Capelli, A., Dual, J., Gaume, J., van Herwijnen, A., Schweizer, J., 2020. Micromechanical modeling of snow failure. Cryosph. 14, 39–49. https://doi.org/10.5194/tc-14-39-2020

Carpinteri, A., 1997. Structural mechanics: a unified approach. Chapman and Hall, London.

Chandel, C., Mahajan, P., Srivastava, P.K., Kumar, V., 2014a. The behaviour of snow under the effect of combined compressive and shear loading. Curr. Sci. 888–894.

Chandel, C., Srivastava, P.K., Mahajan, P., 2015. Determination of failure envelope for faceted snow through numerical simulations. Cold Reg. Sci. Technol. 116, 56–64. https://doi.org/10.1016/j.coldregions.2015.04.009

Chandel, C., Srivastava, P.K., Mahajan, P., 2014b. Micromechanical analysis of deformation of snow using X-ray tomography. Cold Reg. Sci. Technol. 101, 14–23. https://doi.org/10.1016/j.coldregions.2014.01.005

Choupani, N., 2008. Mixed-mode cohesive fracture of adhesive joints: Experimental and numerical studies. Eng. Fract. Mech. 75, 4363–4382. https://doi.org/10.1016/j.engfracmech.2008.04.023

Gaume, J., van Herwijnen, A., Chambon, G., Wever, N., Schweizer, J., 2017. Snow fracture in relation to slab avalanche release: critical state for the onset of crack propagation. Cryosph. 11, 217–228.

Gauthier, D., Jamieson, B., 2008a. Fracture propagation propensity in relation to snow slab avalanche release: Validating the Propagation Saw Test. Geophys. Res. Lett. 35.

https://doi.org/10.1029/2008GL034245

Gauthier, D., Jamieson, B., 2008b. Evaluation of a prototype field test for fracture and failure propagation propensity in weak snowpack layers. Cold Reg. Sci. Technol. 51, 87–97. https://doi.org/10.1016/j.coldregions.2007.04.005

Heierli, J., Gumbsch, P., Zaiser, M., 2008. Anticrack nucleation as triggering mechanism for snow slab avalanches. Science (80-.). 321, 240–243.

Hutchinson, J.W., Suo, Z., 1991. Mixed mode cracking in layered materials. Adv. Appl. Mech. 29, 63–191.

Jamieson, J.B., Johnston, C.D., 1998. Refinements to the stability index for skier-triggered dry-slab avalanches. Ann. Glaciol. 26, 296–302. https://doi.org/10.3189/1998AoG26-1-296-302

Jernkvist, L.O., 2001. Fracture of wood under mixed mode loading II. Experimental investigation of Picea abies. Eng. Fract. Mech. 68, 565–576. https://doi.org/10.1016/S0013-7944(00)00128-4

Kirchner, H.O.K., Michot, G., Narita, H., Suzuki, T., 2001. Snow as a foam of ice: Plasticity, fracture and the brittle-to-ductile transition. Philos. Mag. A 81, 2161–2181. https://doi.org/10.1080/01418610108217141

Krenk, S., 1992. Energy release rate of symmetric adhesive joints. Eng. Fract. Mech. 43, 549–559. https://doi.org/10.1016/0013-7944(92)90198-N

Lim, I.L., Johnston, I.W., Choi, S.K., Boland, J.N., 1994. Fracture testing of a soft rock with semi-circular specimens under three-point bending. Part 2—mixed-mode. Int. J. Rock Mech. Min. Sci. Geomech. Abstr. 31, 199–212. https://doi.org/10.1016/0148-9062(94)90464-2

Mall, S., Murphy, J.F., Shottafer, J.E., 1983. Criterion for mixed mode fracture in wood. J. Eng. Mech. 109, 680–690.

Mantič, V., Távara, L., Blázquez, A., Graciani, E., París, F., 2015. A linear elastic-brittle interface model: application for the onset and propagation of a fibre-matrix interface crack under biaxial transverse loads. Int. J. Fract. 195, 15–38. https://doi.org/10.1007/s10704-015-0043-0

McClung, D.M., 2009. Dry snow slab quasi-brittle fracture initiation and verification from field tests. J. Geophys. Res. Earth Surf. 114. https://doi.org/10.1029/2007JF000913

McClung, D.M., 1977. Direct Simple Shear Tests on Snow and their Relation to Slab Avalanche Formation. J. Glaciol. 19, 101–109. https://doi.org/10.3189/S0022143000215578

McClung, D.M., Schweizer, J., 2006. Fracture toughness of dry snow slab avalanches from field measurements. J. Geophys. Res. Earth Surf. 111. https://doi.org/10.1029/2005JF000403

Mede, T., Chambon, G., Hagenmuller, P., Nicot, F., 2018. Snow Failure Modes Under Mixed Loading. Geophys. Res. Lett. 45. https://doi.org/10.1029/2018GL080637

Nakamura, T., Abe, O., Hashimoto, R., Ohta, T., 2010. A dynamic method to measure the shear strength of snow. J. Glaciol. 56, 333–338. https://doi.org/10.3189/002214310791968502

Narita, H., 1980. Mechanical behaviour and structure of snow under uniaxial tensile stress. J. Glaciol. 26, 275–282. https://doi.org/10.3189/S0022143000010819

Perla, R., Beck, T.M.H., Cheng, T.T., 1982. The shear strength index of alpine snow. Cold Reg. Sci. Technol. 6, 11–20. https://doi.org/10.1016/0165-232X(82)90040-4

Reeder, J.R., 1992. An evaluation of mixed-mode delamination failure criteria.

Reiweger, I., Gaume, J., Schweizer, J., 2015. A new mixed-mode failure criterion for weak snowpack layers. Geophys. Res. Lett. 42, 1427–1432.

Schöttner, J., Piecuch, M., Rosendahl, P.L., Walet, M., Adam, V., Weißgraeber, P., Schweizer, J., van Herwijnen, A., 2026. Testing the Strength of Buried Surface Hoar Weak Layers Under Combined Compression and Shear Loading. Geophys. Res. Lett. 53. https://doi.org/10.1029/2025GL120870

Sigrist, C., Schweizer, J., 2007. Critical energy release rates of weak snowpack layers determined in field experiments. Geophys. Res. Lett. 34. https://doi.org/10.1029/2006GL028576

Sigrist, C., Schweizer, J., Schindler, H.-J., Dual, J., 2006. The energy release rate of mode II fractures in layered snow samples. Int. J. Fract. 139, 461–475. https://doi.org/10.1007/s10704-006-6580-9

Appendix A. Formulations based on Euler-Bernoulli or Timoshenko beam theories

Appendix A.1. Formulation based on Euler-Bernoulli beam theory

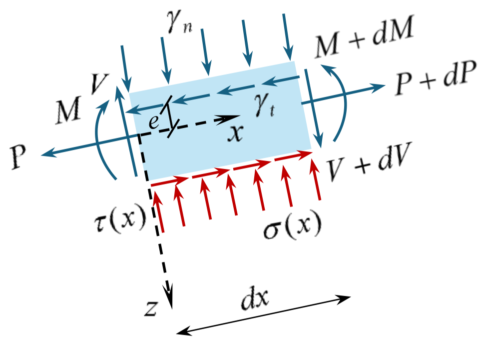

Fig. A1. Free-body diagram of a beam element.

Here, we derive equations for modeling slab as an elastic beam resting on the weak layer as an elastic foundation. The beam is considered within $0 \le x \le L$, with the cut in the weak layer within $L-a \le x \le L$. For a length element dx of the beam, variations in the axial force $P(x)$, shear force $V(x)$, and the moment $M(x)$ in the beam can be related to the reactions of the elastic foundation, i.e. the shear stress $\tau(x)$ and the normal stress $\sigma(x)$, enforcing static equilibrium as:

$$\frac{1}{B}\frac{dP(x)}{dx}+\tau(x)=\gamma_t\,, \tag{A1}$$

$$\frac{1}{B}\frac{dV(x)}{dx}-\sigma(x)+\gamma_n=0\,, \tag{A2}$$

$$\frac{1}{B}\frac{dM(x)}{dx}-\frac{1}{B}V(x)+\left(\frac{H}{2}\tau(x)+e\gamma_t\right)=0\,, \tag{A3}$$

where $\gamma_n=\gamma\cos\phi$ and $\gamma_t=\gamma\sin\phi$ are the normal and tangential components of the total vertical load $\gamma=p_{surf}+\bar{\rho}gH$ which includes both weight of the slab as well as the additional surface loading used in experiments, and B represents width of the slab normal to the xz plane. The term $e\gamma_t$ has been included in Eq. (A3) to account for the fact that the overall tangential component of the resultant loading system may not pass through the centerline of the beam due to the presence of an additional surface loading and/or a nonuniform density profile of slab, hence causing a distributed moment along the beam, where e is the loading eccentricity. For a homogeneous slab with an additional distributed vertical load at the surface, i.e. at $z=-H/2$, $e=\frac{p_{surf}H}{2\gamma}$, which further reduces to $e\approx H/2$ when the surface loading is much larger compared to the weight of the slab, i.e. for $\gamma\approx p_{surf}$. Moreover, the term $\frac{H}{2}\tau(x)$ in Eq. (A3) accounts for the moment caused by the tangential stress of the elastic foundation. Note also the positive directions of $\tau(x)$ and $\sigma(x)$ as shown in Fig. A1.

Using Euler-Bernoulli beam theory, one may introduce axial displacement of the beam as $U(x,z)=u(x)-\frac{dw(x)}{dx}z$ where $u(x)$ represents axial displacement at the centerline of the beam, i.e. $u(x)=U(x,z=0)$, leading to the axial normal strain $\varepsilon_x(x,z)=\frac{du(x)}{dx}-\frac{d^2w(x)}{dx^2}z$. Letting $\sigma(x,z)=E'(z)\varepsilon_x(x,z)$, $E'(z)$ being the depth-variable plane strain elastic modulus of the slab, the total axial force and moment in a cross-section of the beam can be found from:

$$\frac{P(x)}{B}=\int_A \sigma_x(x,z)dz=HE_0'\frac{du(x)}{dx}-H^2E_1'\frac{d^2w(x)}{dx^2}, \tag{A4}$$

$$\frac{M(x)}{B}=\int_A z\sigma_x(x,z)dz=H^2E_1'\frac{du(x)}{dx}-H^3E_2'\frac{d^2w(x)}{dx^2}. \tag{A5}$$

where $E_0'=\frac{1}{H}\int_{-H/2}^{-H/2}E'(z)dz$, $E_1'=\frac{1}{H^2}\int_{-H/2}^{H/2}E'(z)zdz$, $E_2'=\frac{1}{H^3}\int_{-H/2}^{-H/2}E'(z)z^2dz$. Note that $E_1'=0$, and $E_2'=1/12\,E_0'$ for a homogeneous beam. Further, the displacement-traction laws for the elastic foundation can be written as:

$$\sigma(x)=k_n w(x), \tag{A6}$$

$$\tau(x)=-k_t U(x,z=H/2)=-k_t\left(u(x)-\frac{H}{2}\frac{dw(x)}{dx}\right), \tag{A7}$$

where in writing the latter, we have noted that the tangential reaction of the elastic foundation is related to the tangential displacement at the bottom of the beam, i.e. at $z = H/2$. Note that the positive directions of the foundation stresses $\sigma(x)$ and $\tau(x)$ are as shown in Fig. B1, and that the those of $u(x)$ and $w(x)$ are in the positive directions of x and z.

Inserting (A4) and (A7) into Eq. (A1) one arrives at:

$$HE_0' \frac{d^2u(x)}{dx^2} - k_t u(x) - H^2 E_1' \frac{d^3w(x)}{dx^3} + \frac{k_t H}{2}\frac{dw(x)}{dx} = \gamma_t\,. \tag{A8}$$

The second governing equation follows from taking derivative of (A3) with respect to x, replacing $dV(x)/dx$ from (A2), $M(x)$ from Eq. (A5), and $\sigma(x)$ from (A6). The result reads:

$$H^3 E_2' \frac{d^4w(x)}{dx^4} - \frac{k_t H^2}{4}\frac{d^2w(x)}{dx^2} + k_n w(x) - H^2 E_1' \frac{d^3u(x)}{dx^3} + \frac{H}{2}k_t \frac{du(x)}{dx} = \gamma_n\,. \tag{A9}$$

The governing equations (A8) and (A9) are coupled equations for $u(x)$ and $w(x)$ which are to be solved over two regions: (i) $0 \le x \le L-a$ where the beam is bonded to the weak layer with the stiffness of k_t and k_n, and (ii) $L-a \le x \le L$ where the interface is cracked, and hence $k_t = k_n = 0$. To enforce the boundary conditions, we note that the axial force $P(x)$ and the moment $M(x)$ are known in terms of the displacements $u(x)$ and $w(x)$ from Eqs. (A4) and (A5), respectively. Further, the shear force follows from Eq. (A3), once $M(x)$ and $\tau(x)$ are replaced from Eqs. (A5) and (A7) respectively, in the form of:

$$\frac{V(x)}{B} = -H^3 E_2' \frac{d^3w(x)}{dx^3} - \frac{H}{2}k_t u(x) + k_t \frac{H^2}{4}\frac{dw(x)}{dx} + H^2 E_1' \frac{d^2u(x)}{dx^2} + e\gamma_t\,. \tag{A10}$$

The complete solution is then found from setting the axial force, the shear force, and the moment equal to zero at $x = 0$ and $x = L$, and further matching the solutions at $x = L-a$ through imposing continuity of $u(x)$, $w(x)$, $dw(x)/dx$, as well as the continuity of $P(x)$, $V(x)$, and $M(x)$ at $x = L-a$. The energy release rates can then be found from using Krenk's formula (as we have *ab initio* verified from the Griffith energy balance) $G_I = \frac{1}{2}\frac{\sigma_{tip}^2}{k_n}$ and $G_{II} = \frac{1}{2}\frac{\tau_{tip}^2}{k_t}$ (Krenk, 1992), σ_{tip}

and τ_{tip} being reactions of the foundation at the crack tip $x = L - a$, which are analogue of the Irwin's $G - K$ relationship for adhesive joints.

A.2. Formulation based on the Timoshenko beam theory

To derive an analogous formulation allowing for shear deformation in the beam, one can invoke Timoshenko beam theory, where in addition to the displacement components $u(x)$ and $w(x)$ of the beam centerline, an independent function $\psi(x)$ is introduced representing cross-sectional rotation along the beam. Hence, displacement components at each point of the beam can be written as $U(x,z) = u(x) + \psi(x)z$, $W(x,z) = w(x)$, resulting in the axial strain $\varepsilon_x(x,z) = \frac{\partial U(x,z)}{\partial x} = \frac{du(x)}{dx} + \frac{d\psi(x)}{dx}z$ as well as the shear strain $\gamma_{xz}(x) = \psi(x) + \frac{dw(x)}{dx}$. Note that for $\psi(x) = -\frac{dw(x)}{dx}$, the theory reduces to the EB theory with a vanishing shear strain. The axial and shear forces as well as the bending moment are found from:

$$\frac{P(x)}{B} = \int_A \sigma_x(x,z)dz = HE_0' \frac{du(x)}{dx} + H^2 E_1' \frac{d\psi(x)}{dx}, \tag{A11}$$

$$\frac{V(x)}{B} = \kappa \left(\int_A G(z)dz \right) \left(\psi(x) + \frac{dw(x)}{dx} \right) = \kappa G_0 H \left(\psi(x) + \frac{dw(x)}{dx} \right), \tag{A12}$$

$$\frac{M(x)}{B} = \int_A z\sigma_x(x,z)dz = H^2 E_1' \frac{du(x)}{dx} + H^3 E_2' \frac{d\psi(x)}{dx}, \tag{A13}$$

with $G_0 = \frac{1}{H} \int_{-H/2}^{-H/2} G(z)dz$, and κ being the shear correction factor. Using Timoshenko beam theory, Eq. (A6) still remains applicable for the normal reaction of the foundation, however, Eq. (A7) for the tangential reaction now takes on the following form:

$$\tau(x) = -k_t U(x, z = H/2) = -k_t \left(u(x) + \frac{H}{2}\psi(x) \right). \tag{A14}$$

The governing equations then follow from replacing Eqs. (A11)-(A13) into the equilibrium equations (A1)-(A3), and invoking Eqs. (A6) and (A14). The result reads:

$$HE_0' \frac{d^2u(x)}{dx^2} - k_t u(x) + H^2 E_1' \frac{d^2\psi(x)}{dx^2} - \frac{k_t H}{2} \psi(x) = \gamma_t \,, \tag{A15}$$

$$\kappa G_0 H \left(\frac{d\psi(x)}{dx} + \frac{d^2 w(x)}{dx^2} \right) - k_n w(x) + \gamma_n = 0 \,, \tag{A16}$$

$$E_1' H^2 \frac{d^2u(x)}{dx^2} + H^3 E_2' \frac{d^2\psi(x)}{dx^2} - H \left(k_t \frac{H}{4} + \kappa G_0 \right) \psi(x) - \kappa G_0 H \frac{dw(x)}{dx} - k_t \frac{H}{2} u(x) + e\gamma_t = 0 \,. \tag{A17}$$

Eqs. (A15)-(A17) provide three linear differential equations coupled in terms of the unknown functions $u(x)$, $w(x)$, and $\psi(x)$, which are to be solved over the uncracked and cracked segments of the weak layer, respectively within $0 \le x \le L-a$ and $L-a \le x \le L$, in the latter case with $k_t = k_n = 0$ for the latter case. The required boundary conditions at the two ends of the beam follow from setting $P(x)$, $V(x)$, and $M(x)$ from Eqs. (A11)-(A13) equal to zero at $x = 0, L$. The solution over two segments are to be matched at $x = L-a$ by enforcing continuity of deformation $u(x)$, $w(x)$, $\psi(x)$ and continuity of the axial force $P(x)$, shear force $V(x)$, and bending moment $M(x)$ in the beam.

Appendix B. Limit of a rigid slab-elastic weak layer

The bonded length of the weak layer, $L-a$, is subject to the combined action of a normal compressive load N and the moment M. Treating the weak layer as a distributed spring, slab equilibrium requires $\int_0^{L-a}\sigma(x)dx = N$, and $\int_0^{L-a}\sigma(x)\left(x-\frac{L-a}{2}\right)dx = M$, where $\sigma(x)$ is the compressive reaction of the foundation. For a rigid slab, displacement of the elastic foundation varies linearly as $w(x) = w_0 + \omega x$ along the slab, w_0 and ω being constants. Inserting the latter into $\sigma(x) = k_n w(x)$, the two integral equilibrium equations can be solved for w_0 and ω, and the result can be used to find the stress. Of particular interest is the stress at the tip, $x = L-a$, which can be found from:

$$\sigma_{tip} = \frac{6M}{(L-a)^2} + \frac{N}{L-a}. \tag{B1}$$

Replacing $N = W\cos\phi$ and M from Eq. (3) into Eq. (B1) yields:

$$\sigma_{tip} = W\left(\frac{6}{(L-a)^2}\left(\frac{\cos\phi\, a}{2} - \sin\phi H'\right) + \frac{\cos\phi}{L-a}\right). \tag{B2}$$

Further, the shear stress is given by:

$$\tau_{tip} = \frac{T}{L-a} = \frac{W\sin\phi}{L-a}. \tag{B3}$$

The energy release rates can then be found from using Krenk's formula $G_I = \frac{1}{2}\frac{\sigma_{tip}^2}{k_n}$ and $G_{II} = \frac{1}{2}\frac{\tau_{tip}^2}{k_t}$ (Krenk, 1992) which are analogue of the Irwin's $G-K$ relationship for adhesive joints, as we have verified from the *ab initio* Griffith energy balance.

Appendix C. An analytical solution for the energy release rate based on a simplified formulation

A simplified version of the theory enabling analytical derivation of the energy release rate is of interest for identifying the key parameters that regulate transition in failure mode. To this end, we consider a homogeneous slab for which $E_1' = 0$, and also ignore the effect of rotation on the tangential displacement in the elastic foundation equation, i.e. reducing Eq. (A7) to $\tau(x) = -k_t u(x)$. Eqs. (A8), (A9), and (A10) then reduce to:

$$HE_0' \frac{d^2u(x)}{dx^2} - k_t u(x) = \gamma_t , \tag{C1}$$

$$H^3 E_2' \frac{d^4w(x)}{dx^4} + k_n w(x) + \frac{H}{2} k_t \frac{du(x)}{dx} = \gamma_n , \tag{C2}$$

$$\frac{V(x)}{B} = -H^3 E_2' \frac{d^3w(x)}{dx^3} - \frac{H}{2} k_t u(x) + e\gamma_t . \tag{C3}$$

Note that the term $\frac{H}{2} k_t u(x)$ in Eq. (C3) accounts for the distributed bending moment induced by shear stresses at the weak layer, with its derivative appearing in Eq. (C2). This distributed moment which varies with x is only present within $0 \le x \le L-a$, and vanishes for $L-a \le x \le L$ where the interface is cracked. For analytical tractability, we introduce the approximation $u(x) \approx \bar{u}$ where $\bar{u} = \frac{1}{L-a}\int_0^{L-a} u(x)dx = \frac{-\gamma_t L}{k_t(L-a)}$ is the average value of $u(x)$ within the uncracked segment. Here, we have used the fact that $u(x) = -\tau(x)/k_t$, and the global equilibrium condition $\int_0^{L-a} \tau(x)dx = \gamma_t L$. Setting $u(x) \approx \bar{u}$, Eq. (C2) reduces to:

$$H^3 E_2' \frac{d^4w(x)}{dx^4} + k_n w(x) = \gamma_n . \tag{C4}$$

Further, Eq. (C3) can be written as:

$$\frac{V(x)}{B} = -H^3 E_2' \frac{d^3w(x)}{dx^3} + \frac{H}{2} \frac{\gamma_t L}{(L-a)} + e\gamma_t , \text{ for } 0 \le x \le L-a , \tag{C5}$$

$$\frac{V(x)}{B}=-H^3E_2'\frac{d^3w(x)}{dx^3}+e\gamma_t\text{, for } L-a\le x\le L. \tag{C6}$$

It is worth noting that the formulation obtained here is essentially equivalent to considering the beam, in addition to the normal and tangential loadings, subject to a uniform distributed moment $e\gamma_t$ acting within $L-a\le x\le L$ and a uniform distributed moment $\frac{H}{2}\frac{\gamma_t L}{(L-a)}+e\gamma_t$ within $0\le x\le L-a$.

The governing Eqs. (C1) and (C4) subject to the boundary conditions, $P=V=M=0$ at both ends, $x=0,L$, as well as continuity of $u(x)$, $w(x)$, $dw(x)/dx$, $P(x)$, $V(x)$, and $M(x)$ at $x=L-a$, can be solved analytically. Of particular interest are displacements at the crack tip, $u_{tip}=u(x=L-a)$ and $w_{tip}=w(x=L-a)$ which can be used for funding the energy release rate as $G=\frac{1}{2}k_n w_{tip}^2+\frac{1}{2}k_t u_{tip}^2$. The result can be cast in the form of Eq. (9) where:

$$g_I(\hat{a},\hat{\lambda}_n;\phi,\eta_1,H/L)=\left(\frac{A_1(\hat{a},\hat{\lambda}_n;\phi,\eta_1)+A_2'(\hat{a},\hat{\lambda}_n;\phi,\eta_1,H/L)}{\left(F_1(\hat{a},\hat{\lambda}_n)-2\right)(1-\hat{a})}\right)^2, \tag{C7}$$

$$g_{II}(\hat{a},\hat{\lambda}_t)=\left(-1+\hat{a}\hat{\lambda}_t\coth\left[\left(\hat{a}-1\right)\hat{\lambda}_t\right]\right)^2, \tag{C8}$$

$$A_1(\hat{a},\hat{\lambda}_n;\phi,\eta_1)=(1-\hat{a})\left(-2+F_1(\hat{a},\hat{\lambda}_n)-\left(\hat{a}^2-2\hat{a}\eta_1\tan\phi\right)\hat{\lambda}_n^2F_{-1}(\hat{a},\hat{\lambda}_n)\right), \tag{C9}$$

$$A_2'\left(\hat{a},\hat{\lambda}_n;\phi,\eta_1,\frac{H}{L}\right)=\hat{\lambda}_n\tan\phi\left(\frac{H}{L}+2\eta_1-2\hat{a}\eta_1\right)\left(2F_2(\hat{a},\hat{\lambda})-F_4(\hat{a},\hat{\lambda}_n)\right)+F_4(\hat{a},\hat{\lambda}_n)\hat{\lambda}_n\left(2\hat{a}-2\hat{a}^2\right), \tag{C10}$$

$$F_{\pm1}\left(\hat{a},\hat{\lambda}_n\right)=\cos\left[2\left(\hat{a}-1\right)\hat{\lambda}_n\right]\pm\cosh\left[2\left(\hat{a}-1\right)\hat{\lambda}_n\right], \tag{C11}$$

$$F_2(\hat{a},\hat{\lambda}_n)=\cosh\left[\left(\hat{a}-1\right)\hat{\lambda}_n\right]\sin\left[\left(\hat{a}-1\right)\hat{\lambda}_n\right]-\cos\left[\left(\hat{a}-1\right)\hat{\lambda}_n\right]\sinh\left[\left(\hat{a}-1\right)\hat{\lambda}_n\right], \tag{C12}$$

$$F_4(\hat{a},\hat{\lambda}_n)=\sin\left[2\left(\hat{a}-1\right)\hat{\lambda}_n\right]-\sinh\left[2\left(\hat{a}-1\right)\hat{\lambda}_n\right], \tag{C13}$$

where $\hat{a} = \dfrac{a}{L}$, $\hat{\lambda}_n = \left(\dfrac{(1-\nu^2)k_n}{4E\bar{I}} \right)^{1/4} L$, $\hat{\lambda}_t = \left(\dfrac{(1-\nu^2)k_t}{EH} \right)^{1/2} L$, $\eta_1 = e/L$.